Nonlinear Response of Atmospheric Vortices to Heating by Organized Cumulus Convection

JAMES J. HACK

National Center for Atmospheric Research, Boulder, CO 80307*

WAYNE H. SCHUBERT

Department of Atmospheric Science, Colorado State University, Fort Collins, CO 80523

(Manuscript received 9 August 1985, in final form 6 February 1986)

ABSTRACT

Using an axisymmetric primitive-equation tropical cyclone model, we first illustrate the way in which nonlinear processes contribute to the development of an atmospheric vortex. These numerical experiments show that nonlinearities allow a given diabatic heat source to induce larger tangential wind (and kinetic energy) changes as the vortex develops and the inertial stability becomes large. In an attempt to gain a deeper theoretical understanding of this process, we consider the energy cycle in the balanced vortex equations of Eliassen. The temporal behavior of the total potential energy P is governed by $dP/dt = H - C$, where H is the rate of generation of total potential energy by diabatic heating, and C is the rate of conversion to kinetic energy. We define a time-dependent system efficiency parameter as $\bar{\eta}(t) = C/H$. Then, using the dynamical simplifications of balanced vortex theory, we express $\bar{\eta}(t)$ as a weighted average of a dynamic efficiency factor $\eta(r, z, t)$. The dynamic efficiency factor is a measure of the efficacy of diabatic heating at any point in generating kinetic energy and can be determined by solving a second-order partial differential equation whose coefficients and right-hand side depend only on the instantaneous vortex structure. The diagnostic quantities $\bar{\eta}(t)$ and $\eta(r, z, t)$ are utilized in the analysis of several balanced numerical experiments with different vertical and radial distributions of a diabatic heat source.

1. Introduction

For many years, tropical meteorologists have wrestled with the question of how the relatively common tropical cloud cluster is transformed into the more infrequently observed hurricane or typhoon. Charney and Eliassen (1964) and Ooyama (1964) were the first to propose a closed theory describing the dynamical events responsible for this transformation, most frequently referred to as Conditional Instability of the Second Kind, or CISK. This theory proposes that tropical cyclone development occurs due to a secondary instability involving the cooperative interaction of two scales of motion. The convective-scale motions provide a horizontal gradient of latent heat release which forces a large-scale secondary radial circulation. This large-scale radial circulation provides the convective-scale with the necessary moisture through the horizontal influx of water vapor in the lower levels. As the large-scale circulation increases, so does the horizontal transport of water vapor, which serves to increase the release of latent energy in the inner regions which, in turn, further intensifies the large-scale circulation.

The limited observational data available on tropical cyclone structure (e.g., see Gray, 1981) suggest that the total amount of water processed by the cloud cluster and the fully developed tropical storm is about the same in an area-averaged sense. Only the horizontal distribution of the total latent heat release is different. These data and the results of nonlinear numerical simulations of the tropical cyclone life cycle do not entirely support the linear CISK hypothesis, which relies on increased convection and the associated increase in precipitation (i.e., convective heating) for development. Although the theory provides an adequate explanation of the gross conceptual features of tropical cyclone genesis, it appears to be incomplete, given observational and nonlinear numerical evidence.

This raises the question of just how the atmosphere responds dynamically to the release of latent heat in tropical cloud clusters. This response can depend on many factors, including the latitude of the disturbance, the horizontal scale of the heating, and the static and inertial stabilities of the flow in which the heating is embedded. The first two factors can be studied using linear models on an f-plane (e.g., Schubert et al., 1980) or an equatorial β-plane (e.g., Silva Dias et al., 1983). The remaining factors are essentially nonlinear because the static and inertial stabilities (and therefore the response) change as the flow field evolves. In particular,

* The National Center for Atmospheric Research is sponsored by the National Science Foundation.

© 1986 American Meteorological Society

the pressure fall and tangential wind acceleration produced by a heat source imbedded in a strong vortex can be much larger than the corresponding changes produced by the same heat source in a weak vortex (Shapiro and Willoughby, 1982; Ooyama, 1982; Schubert and Hack, 1982).

In order to establish a feeling for the role of these nonlinear effects on the development of a tropical vortex, let us consider the following numerical experiments performed with two simplified versions of an 18-level, axisymmetric, primitive-equation, sigma-coordinate hurricane model (see Hack, 1980). For the convenience of later discussion, we will present the continuous governing equations in a pseudo-height coordinate (cf., Hoskins and Bretherton, 1972). The axisymmetric, f-plane, inviscid response to a specified heat source $\mathbf{Q}(r, z, t)$ is then determined by the system of equations given by

$$\frac{\partial u}{\partial t} + \underline{u\frac{\partial u}{\partial r}} + \underline{w\frac{\partial u}{\partial z}} - \left(f + \underline{\frac{v}{r}}\right)v + \frac{\partial \phi}{\partial r} = 0, \quad (1.1)$$

$$\frac{\partial v}{\partial t} + \underline{u\frac{\partial v}{\partial r}} + \underline{w\frac{\partial v}{\partial z}} + \left(f + \underline{\frac{v}{r}}\right)u = 0, \quad (1.2)$$

$$\frac{\partial \phi}{\partial z} = \frac{g}{\theta_0}\theta, \quad (1.3)$$

$$\frac{\partial ru}{r\partial r} + \frac{\partial \rho w}{\rho \partial z} = 0, \quad (1.4)$$

$$\frac{\partial \ln\theta}{\partial t} + \underline{u\frac{\partial \ln\theta}{\partial r}} + w\frac{\partial \ln\theta}{\partial z} = \frac{\mathbf{Q}}{c_p T}, \quad (1.5)$$

where $z \equiv [1 - (p/p_0)^\kappa](c_p\theta_0/g)$ is the pseudo-height, $\rho(z)$ is a known pseudo-density, u, v, w are the radial, tangential, and vertical components of velocity, θ the potential temperature, and ϕ the geopotential. We shall refer to the system (1.1)–(1.5) as the *nonlinear model.* Neglecting all the underlined terms in (1.1)–(1.5) and replacing $\partial \ln\theta/\partial z$ with a specified mean tropical profile $\partial \ln\bar{\theta}/\partial z$ result in a system which will be referred to as the *linear model.* We wish to illustrate the different responses produced by each of these model formulations by assuming they are forced with a specified invariant heat source of the form

$$\frac{\mathbf{Q}}{c_p}(r, z) = aQ_1(z)e^{-(r/r_0)^2}. \quad (1.6)$$

For these experiments, $Q_1(z)$ is an analytic approximation to the apparent heat source obtained by Yanai et al. (1973). In the pressure coordinate, it takes the form

$$Q_1(p) = \hat{Q}\sin(\pi\sigma)e^{-\alpha\sigma}, \quad (1.7)$$

where

$$\sigma \equiv \frac{p - p_T}{p_B - p_T}, \quad (1.8)$$

and the pressure surfaces bounding the heated region have been chosen to be $p_B = 1000$ mb ($z = 0$) and $p_T = 100$ mb ($z = 14.8$ km). This formulation allows the vertical location of the heating maximum to be easily displaced, while at the same time maintaining a constraint on the vertically integrated heating. Choosing $\hat{Q} = 7.87°\text{C day}^{-1}$ and $\alpha = 0.554$ places the maximum heating at 500 mb ($z = 5.5$ km), which proves to be a very good approximation to the Yanai heating profile. The normalization coefficient a is determined by requiring the horizontally averaged heating inside radius r_1 to be equal to $Q_1(z)$. This is mathematically equivalent to requiring

$$a = \frac{r_1^2}{2\int_0^{r_1} re^{-(r/r_0)^2}dr} = \left(\frac{r_1}{r_0}\right)^2[1 - e^{-(r_1/r_0)^2}]^{-1}. \quad (1.9)$$

For the experiments to be presented, we have chosen $r_1 = 250$ km and $r_0 = 150$ km. Although the instantaneous switch-on of the heating at $t = 0$ excites some transient gravity wave energy, it quickly leaves the computational domain by means of a radiation boundary condition (Hack and Schubert, 1981).

In Figs. 1 and 2, the time evolution of the central surface pressure, the maximum tangential wind, and the radius of maximum tangential wind are shown for the linear (dashed lines) and the nonlinear (solid lines) models. The linear model produces a vortex with a fixed radius of maximum wind (160 km), a central surface pressure tendency of 0.75 mb day^{-1}, and a maximum tangential wind change of about 3 m s^{-1} day^{-1}. The nonlinear model produces a vortex which begins to deviate significantly from the linear solution after 24 h. As the radius of maximum wind moves inward, the central surface pressure and the maximum tangential wind begin to change more rapidly. Near the end of the five-day integration, the surface pressure tendency in the nonlinear model is about twenty times that produced by the linear model, while the maximum tangential wind change is three times the linear rate.

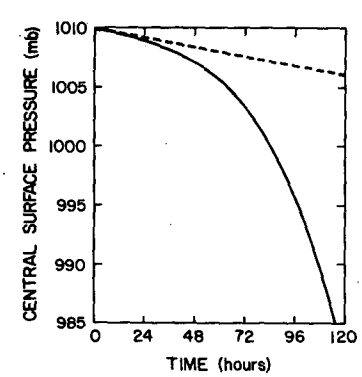

FIG. 1. Central surface pressure as a function of time for an invariantly forced linear primitive-equation model (dashed) and nonlinear primitive-equation model.

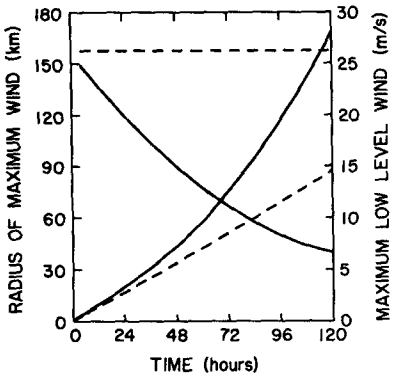

FIG. 2. Radius of maximum wind and maximum low-level tangential wind as a function of time for an invariantly forced linear primitive-equation model (dashed) and nonlinear primitive-equation model (also see Fig. 1).

In general, the nonlinear response to this artificial forcing is much more analogous to the type of behavior observed in developing hurricanes and typhoons (e.g., see Holliday and Thompson, 1979; Kurihara and Tuleya, 1974).

These results demonstrate that nonlinear terms in the governing equations begin to play a significant role in the development of a tropical vortex at a very early stage in its evolution. Unfortunately, it is very difficult to determine what dynamical processes are of most physical significance in primitive-equation results like those presented above. For that reason, in the remainder of this paper we shall attempt to understand the nonlinear behavior observed in the primitive-equation integration using the transformed Eliassen balanced vortex model introduced by Schubert and Hack (1983). The most important benefit of the balanced system is that it allows us to derive an analytic measure of the efficiency of an axisymmetric vortex at converting total potential energy (e.g., generated by latent heat release) to the kinetic energy of the balanced flow. We will show that this dynamic efficiency factor can be simply evaluated from knowledge of the instantaneous flow field. By conducting several numerical experiments with the balanced system and using these diagnostic concepts of efficiency, we hope to provide better insight into the dynamical processes that contribute to the nonlinear response observed in the primitive-equation results discussed above.

2. Review of balanced vortex theory

Let us now consider axisymmetric flows which are always close to a state of gradient balance, so that (1.1) can be approximated by $[f + (v/r)]v = \partial\phi/\partial r$. A necessary condition for this to be true is that the forcing have a time scale that is large when compared to $1/f$. In the absence of friction, the absolute angular momentum per unit mass

$$\frac{f}{2}R^2 = rv + \frac{f}{2}r^2$$

is conserved. We call R the potential radius, i.e., the radius to which a parcel must be moved (conserving absolute angular momentum) in order to change its tangential component of velocity to zero. The governing equations then become (2.1)–(2.5) of Table 1.

TABLE 1. Governing equations.

$$\frac{1}{4}f^2\frac{(R^4 - r^4)}{r^3} = \frac{\partial\phi}{\partial r}, \tag{2.1}$$

$$\frac{1}{2}f^2R\left(\frac{R^2 - r^2}{r^2}\right) = \frac{\partial\Phi}{\partial R}, \tag{2.6}$$

$$\frac{\partial}{\partial t}\left(\frac{R^2}{2}\right) + u\frac{\partial}{\partial r}\left(\frac{R^2}{2}\right) + w\frac{\partial}{\partial z}\left(\frac{R^2}{2}\right) = 0, \tag{2.2}$$

$$\frac{\partial}{\partial T}\left(\frac{r^2}{2}\right) - Ru^* = 0, \tag{2.7}$$

$$\frac{g}{\theta_0}\theta = \frac{\partial\phi}{\partial z}, \tag{2.3}$$

$$\frac{g}{\theta_0}\theta = \frac{\partial\Phi}{\partial Z}, \tag{2.8}$$

$$\frac{\partial ru}{r\partial r} + \frac{\partial\rho w}{\rho\partial z} = 0, \tag{2.4}$$

$$\frac{\partial Ru^*}{R\partial R} + \frac{\partial\rho w^*}{\rho\partial Z} = 0, \tag{2.9}$$

$$\frac{\partial\theta}{\partial t} + u\frac{\partial\theta}{\partial r} + w\frac{\partial\theta}{\partial z} = \frac{\theta}{c_pT}\mathbf{Q} = Q. \tag{2.5}$$

$$\frac{\partial\theta}{\partial T} + \frac{\theta_0}{g}q\rho w^* = Q. \tag{2.10}$$

We now wish to transform (2.1)–(2.5) from (r, z, t) space to (R, Z, T) space, where $Z = z$ and $T = t$. The upper-case symbols for pseudo-height and time are introduced to distinguish derivatives at constant radius ($\partial/\partial z$ and $\partial/\partial t$) from derivatives at constant potential radius ($\partial/\partial Z$ and $\partial/\partial T$). Derivatives with respect to r and R are related by

$$\frac{\partial}{r\partial r} = \frac{\zeta}{fR}\frac{\partial}{\partial R}, \tag{2.11}$$

where the absolute vorticity ζ is given by

$$\frac{\zeta}{f} = \frac{\partial}{r\partial r}\left(\frac{R^2}{2}\right) \quad \text{or} \quad \frac{f}{\zeta} = \frac{\partial}{R\partial R}\left(\frac{r^2}{2}\right). \tag{2.12}$$

For further discussion on the use of such coordinate transformations, the reader is referred to the work of Shutts and Thorpe (1978), Shutts (1980), Gill (1981), Schubert and Hack (1983) and Thorpe (1985).

In analogy with semigeostrophic theory (Hoskins and Draghici, 1977), we introduce the potential function

$$\Phi = \phi + \frac{1}{2}v^2 = \phi + \frac{1}{8}f^2\frac{(R^2 - r^2)^2}{r^2}, \tag{2.13}$$

and the new transverse circulation components

$$Ru^* = r\left(u - w\frac{\partial r}{\partial Z}\right), \tag{2.14}$$

$$w^* = \frac{f}{\zeta}w. \tag{2.15}$$

Then, as discussed more fully in Schubert and Hack (1983), the governing system (2.1)–(2.5) becomes (2.6)–(2.10), which is shown on the right side of Table 1 for easy comparison. The potential vorticity q is defined below in (2.24a). In comparing the two columns of Table 1, we note that (2.6)–(2.10) represent a simplification over (2.1)–(2.5), since the mathematical forms of the hydrostatic and continuity equations have remained essentially unchanged while the gradient, tangential momentum, and thermodynamic equations have all been considerably simplified.

Although the system (2.1)–(2.5) is closed in the unknowns u, R, w, θ, ϕ, and the system (2.6)–(2.10) is closed in the unknowns u^*, r, w^*, θ and Φ, they are not in forms convenient for numerical integration. More suitable forms can be obtained in one of two ways. The first method involves replacing one of the prognostic equations, (2.2) or (2.5), with a diagnostic relation for the transverse circulation (ρu, ρw). Similarly, in the transformed system one of the prognostic equations (2.7) or (2.10) can be replaced with a diagnostic equation for the transverse circulation (ρu^*, ρw^*). The second method involves elimination of the transverse circulation components to obtain elliptic equations for ϕ_t and Φ_T. This method is presented in Schubert et al. (1984) and Thorpe (1985) and will not be discussed here.

To derive the transverse circulation equation for the system (2.1)–(2.5), we first substitute (2.3) into (2.5) and (2.1) into (2.2) to obtain

$$\phi_{zt} + A\rho w - B\rho u = \frac{g}{\theta_0}Q, \tag{2.16}$$

$$\phi_{rt} - B\rho w + C\rho u = 0, \tag{2.17}$$

where

$$\rho A = \frac{g}{\theta_0}\frac{\partial\theta}{\partial z}, \tag{2.18a}$$

$$\rho B = -\frac{g}{\theta_0}\frac{\partial\theta}{\partial r} = -f^2\frac{R^3}{r^3}\frac{\partial R}{\partial z}, \tag{2.18b}$$

$$\rho C = f^2\frac{R^3}{r^3}\frac{\partial R}{\partial r}. \tag{2.18c}$$

Using the continuity equation (2.4) to define a streamfunction ψ so that

$$(\rho u, \rho w) = \left(-\frac{\partial\psi}{\partial z}, \frac{\partial r\psi}{r\partial r}\right), \tag{2.19}$$

and eliminating the tendency terms between (2.16) and (2.17), we obtain the transverse circulation equation

$$\mathbf{L}\psi = \frac{g}{\theta_0}\frac{\partial Q}{\partial r}, \tag{2.20}$$

where

$$\mathbf{L}(\ ) = \frac{\partial}{\partial r}\left(A\frac{\partial r(\ )}{r\partial r} + B\frac{\partial(\ )}{\partial z}\right) + \frac{\partial}{\partial z}\left(B\frac{\partial r(\ )}{r\partial r} + C\frac{\partial(\ )}{\partial z}\right). \tag{2.21}$$

The boundary conditions for (2.21) are that $\psi = 0$ on the top, bottom, and inner boundaries, and that $\psi \to 0$ as $r \to \infty$.

Equation (2.20) was first derived by Eliassen (1952), who discussed the characteristics of the transverse circulation resulting from point sources and jumps in the forcing, which appears on the right-hand side. The coefficients A, B and C physically represent the static or gravitational stability, baroclinity, and inertial stability of the vortex, respectively. As shown by Eliassen (1952), air parcels move in the (r, z) plane in response to sources of heat against two stabilizing influences: static stability, which provides resistance to vertical displacements, and inertial stability, which provides resistance to radial displacements. The system of equations given by (2.2) and (2.20), along with necessary auxiliary relations, is sometimes referred to as the quasi-balanced prognostic system and has been successfully used to simulate the time evolution of axisymmetric tropical disturbances (e.g., Ooyama, 1969a,b; Sundqvist, 1970). The major advantage of this system is that the transient aspects of geostrophic or gradient adjustment (i.e., gravity wave motions) are filtered. The balanced system also makes it easier to see how the transverse circulation is nonlinearly coupled with the thermodynamic and tangential momentum fields through the variable coefficients A, B and C.

In linear CISK theory, the governing equations are linearized about a basic state at rest. Consequently, the baroclinity term drops out of the problem, while the inertial stability term is approximated by f^2, and the static stability term is a property of the basic state. Although this approximation may be acceptable for the very early stages of tropical cyclone genesis, its applicability over the whole range of tropical cyclone de-

velopment is certainly questionable. It seems obvious that a linear approach to the problem of tropical cyclone development cannot begin to provide a complete picture of the important dynamical processes contributing to intensification and structure.

To derive the transverse circulation equation for the radially transformed system (2.6)–(2.10), we follow a similar procedure. First substitute (2.8) into (2.10) and (2.6) into (2.7) to obtain

$$\Phi_{ZT} + q\rho w^* = \frac{g}{\theta_0} Q, \tag{2.22}$$

$$\Phi_{RT} + s\rho u^* = 0, \tag{2.23}$$

where the potential vorticity q and the inertial stability s are given by

$$\rho q = \frac{\zeta}{f}\frac{g}{\theta_0}\frac{\partial\theta}{\partial Z}, \tag{2.24a}$$

$$\rho s = f^2 \frac{R^4}{r^4}. \tag{2.24b}$$

Using the continuity equation (2.9) to define a streamfunction ψ^* so that

$$(\rho u^*, \rho w^*) = \left(-\frac{\partial\psi^*}{\partial Z}, \frac{\partial R\psi^*}{R\partial R}\right), \tag{2.25}$$

and eliminating the tendency terms between (2.22) and (2.23), we obtain the transverse circulation equation

$$\mathbf{L}^*\psi^* = \frac{g}{\theta_0}\frac{\partial Q}{\partial R}, \tag{2.26}$$

where

$$\mathbf{L}^*(\quad) = \frac{\partial}{\partial R}\left(q\frac{\partial R(\quad)}{R\partial R}\right) + \frac{\partial}{\partial Z}\left(s\frac{\partial(\quad)}{\partial Z}\right). \tag{2.27}$$

The boundary conditions for (2.26) are that $\psi^* = 0$ on the top, bottom, and inner boundaries and that $\psi^* \to 0$ as $R \to \infty$.

Note that the form of the diagnostic equation in the transformed system has been greatly simplified since it contains no cross-derivative terms; q plays the role of static stability, and s the role of inertial stability. As long as the vortex remains stable, i.e., $q > 0$ and $s > 0$, (2.26) will remain elliptic. In the time integrations that are presented in section 4, we have chosen to use the prognostic equation (2.7) and the diagnostic equation (2.26) for ψ^* along with other necessary diagnostic relations (see Appendix). In addition to the advantage of being mathematically simpler, this system can be solved using fewer degrees of freedom in the horizontal because the inner core region is automatically stretched as the model vortex develops.

One additional comment is that by using (2.11), (2.15), (2.19) and (2.25), we can easily show that $R\psi^* = r\psi$. Thus, isolines of $R\psi^*$ drawn in the (R, Z) plane give the transverse mass flux $(\rho Ru^*, \rho Rw^*)$ while the same isolines drawn in the (r, z) plane (thus distorted) give the transverse mass flux $(\rho ru, \rho rw)$.

3. Energetics and efficiency

From the balanced system, we can derive the following energy equations

$$\frac{dP}{dt} = H - C, \tag{3.1}$$

$$\frac{dK}{dt} = C, \tag{3.2}$$

where

$$P = \iint c_p T\rho r dr dz, \tag{3.3}$$

$$K = \iint \frac{1}{2} v^2 \rho r dr dz, \tag{3.4}$$

$$H = \iint \mathbf{Q}\rho r dr dz, \tag{3.5}$$

$$C = \iint \frac{g}{\theta_0} w\theta\rho r dr dz. \tag{3.6}$$

The radial integrals in (3.3)–(3.6) extend from r equals zero to some large but finite radius, and the vertical integrals from z equals zero to z_T. Thus, P and K denote the total potential and kinetic energies of the atmosphere, H the total heating, and C the rate of conversion of total potential energy into kinetic energy.

Because w is diagnostically related to $\mathbf{Q}$, it is possible to express C in a form similar to H. Although this can be accomplished in either (r, z) space or (R, Z) space, we shall proceed using the (R, Z) formulation for mathematical convenience. With the relations (2.11) and (2.15), we can write (3.6) as

$$C = \iint \frac{g}{\theta_0} w^*\theta\rho R dR dZ. \tag{3.7}$$

Using (2.25) and integrating by parts, (3.7) becomes

$$C = -\iint \psi^* \frac{g}{\theta_0}\frac{\partial\theta}{\partial R} R dR dZ. \tag{3.8}$$

In analogy with Eliassen (1952), let us now define χ^* to be the solution of

$$\mathbf{L}^*\chi^* = \frac{g}{\theta_0}\frac{\partial\theta}{\partial R}, \tag{3.9}$$

with the same homogeneous boundary conditions as (2.26). We can interpret χ^* as the streamfunction for a transverse displacement field. This field does not directly depend on the heating, but only on the instantaneous vortex structure. Substituting (3.9) into (3.8), we obtain

$$C = -\iint \psi^*\mathbf{L}^*\chi^* R dR dZ = -\iint \chi^*\mathbf{L}^*\psi^* R dR dZ. \tag{3.10}$$

The last step follows from the self-adjoint property of

the linear operator $\mathbf{L}^*$. Using (2.26) in (3.10) and performing a final integration by parts, we obtain

$$C = \iint \eta^* \mathbf{Q} \rho R dR dZ, \tag{3.11}$$

where

$$\rho\eta^* = \left(\frac{c_p\theta_0}{g} - Z\right)^{-1} \frac{\partial R\chi^*}{R\partial R}. \tag{3.12}$$

By analogy with (2.15), we define

$$\eta = \frac{\zeta}{f}\eta^*, \tag{3.13}$$

so that (3.11) can be expressed in (r, z) space as

$$C = \iint \eta \mathbf{Q} \rho r dr dz. \tag{3.14}$$

Using (3.5) and (3.14), we can define

$$\bar{\eta} = \frac{C}{H} = \frac{\iint \eta \mathbf{Q} \rho r dr dz}{\iint \mathbf{Q} \rho r dr dz}, \tag{3.15}$$

as the overall efficiency of the energy conversion.

In analogy with Lorenz (1967, p. 105), we shall refer to $\eta(r, z, t)$ as the *dynamic* efficiency factor (in contrast with the thermodynamic efficiency factor introduced by Lorenz and discussed by Johnson, 1970) and $\bar{\eta}(t)$ as the system efficiency. According to (3.15), the dynamic efficiency factor is a measure of the effectiveness of the heating at any point in producing kinetic energy. The functions $\eta(r, z, t)$ and $\bar{\eta}(t)$ are useful diagnostics which can aid in the interpretation of observational data as well as numerical modeling results (both balanced and primitive-equation assuming an approximate balance exists).

4. Numerical integrations

a. Time evolution of $\eta(r, z)$

In this section, we present the results of several numerical integrations using the transformed balanced system discussed in section 2. Details concerning the numerical methods utilized in the solution of this system of equations are presented in the Appendix. We begin by reproducing the results of the nonlinear primitive-equation experiment presented in section 1 where the heating is a prescribed function of space and invariant in time. The time evolution of the magnitude and radial location of the maximum low-level tangential wind for the transformed balanced system are shown by the solid lines in Fig. 3. The results of this balanced experiment are nearly identical to the primitive-equation results, producing a slightly stronger vortex (about 1 m s^{-1} difference) by 120 hours. The final radius of maximum wind is also somewhat smaller, but this is more the result of increased resolution associated with a stretching of the radial coordinate in the interior low levels (see Schubert and Hack, 1983). The two-dimensional structure of the vortex is also quite similar to the primitive-equation solution where the largest observed difference is a slightly smaller radial position of the peak in the upper-level anticyclonic circulation.

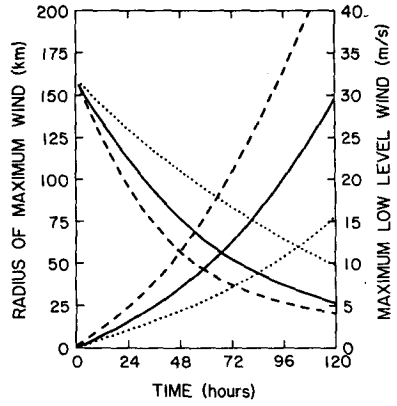

FIG. 3. Radius of maximum wind and maximum low-level tangential wind as a function of time for the invariantly forced balance system. Dotted lines correspond to a maximum forcing at 400 mb, solid lines correspond to maximum forcing at 500 mb, and dashed lines correspond to maximum forcing at 600 mb.

The primitive-equation experiments presented in section 1 suggested that nonlinearities enable a large-scale atmospheric vortex to become more efficient at converting total potential energy (which is generated by convective-scale diabatic heating) to the kinetic energy of the quasi-balanced flow. In section 3, we introduced the mathematical concept of a dynamic efficiency factor, denoted by the variable η. This field can be readily diagnosed from knowledge of the instantaneous large-scale tangential momentum field, which in our analysis is uniquely related to the thermodynamic field by means of thermal wind balance. Therefore, if we have interpreted the primitive-equation solutions correctly, we should see significant changes in this dynamic efficiency factor as our balanced model vortex develops.

The time evolution of the tangential circulation for the balanced experiment is shown in Figs. 4 and 5, along with the corresponding η field. As suggested by our primitive-equation experiments, the η field and the system efficiency $\bar{\eta}$ dramatically increase in magnitude as the vortex circulation intensifies. At 24 hours, the η field has a maximum amplitude of just over 0.5 percent in the center of the vortex at a height of 10 km (approximately 250 mb). As the model vortex circulation strengthens, the dynamic efficiency factor grows in both magnitude and vertical extent in response to large increases in potential vorticity, inertial stability, and the radial temperature gradient in the low to midtroposphere. By the end of the numerical integration at 120 hours, the dynamic efficiency factor has reached a peak value of slightly more than 10 percent in the interior

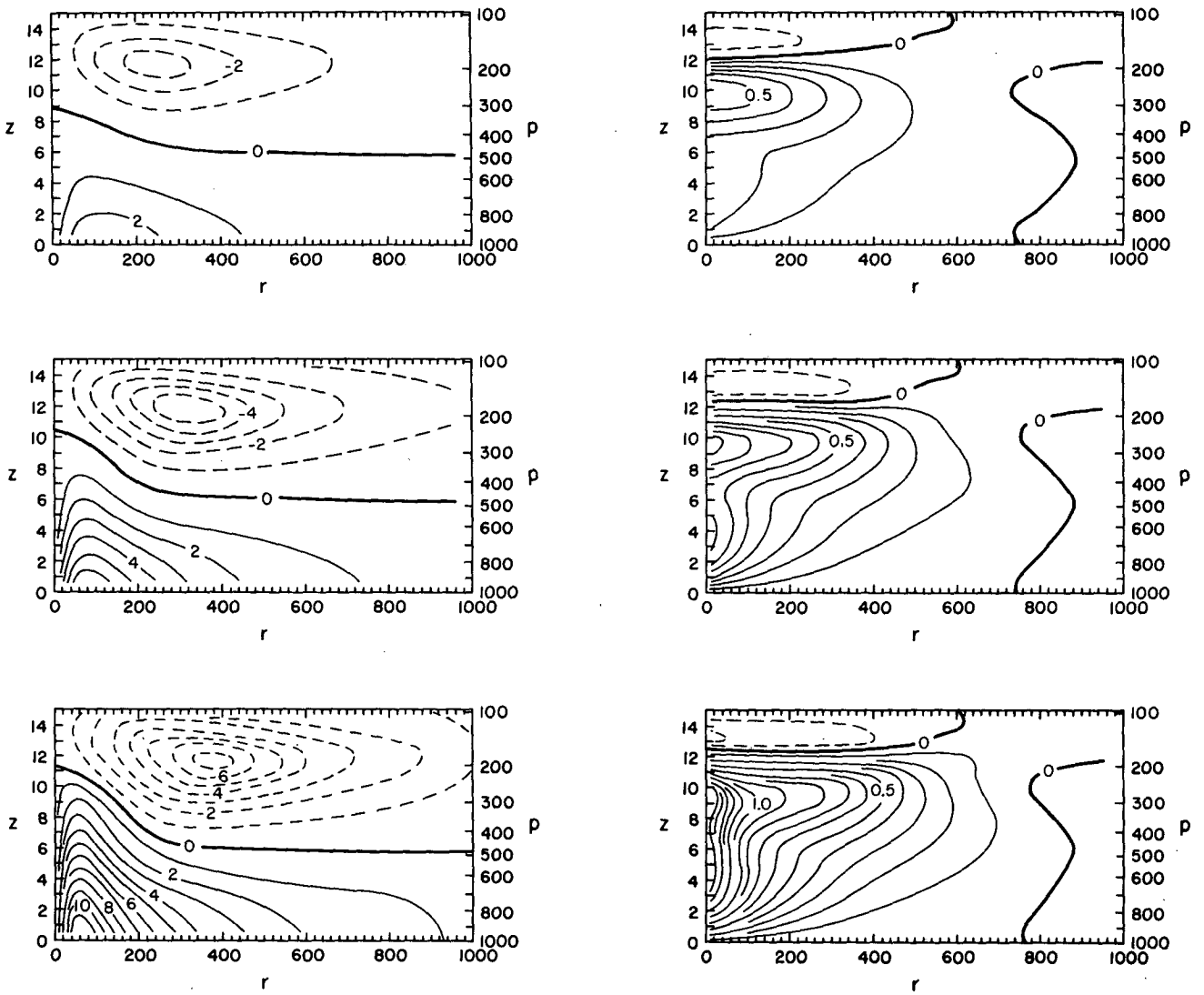

FIG. 4. Tangential momentum (left set of panels) and dynamic efficiency factor $\eta(r, z)$ in the region $r = 0$ to $r = 1000$ km at 24, 48 and 72 hours for the invariantly forced balance model. The contour interval is 1 m s^{-1} for the momentum field and 0.1 percent for the dynamic efficiency factor. Negative values are denoted by dashed lines. See text for further discussion.

upper troposphere of the model vortex, exceeding 2 percent for the majority of the region inside 50 km. During the period from 12 to 120 hours, the system efficiency $\bar{\eta}$ linearly increases from slightly more than 0.1 percent to approximately 1.25 percent (see Fig. 6). At the same time, we observe that the kinetic energy of the system grows quadratically with respect to time, a result that is energetically consistent with the linear growth rate of $\bar{\eta}$.

These results confirm the hypothesis that, as a large-scale atmospheric vortex grows in intensity, its ability to extract kinetic energy from latent heat released in deep cumulus convection also increases. This increase in efficiency contributes to an interesting nonlinear coupling between the large-scale circulation and its response to diabatic heating. The dynamic efficiency factor, which is completely determined by the instantaneous global structure of the tangential circulation, determines how the tangential circulation responds to a diabatic heat source, which in turn further modifies the dynamic efficiency factor. This nonlinear feedback is what is responsible for the hurricane-like solution, despite the fact that the time evolution of the diabatic heat source is completely decoupled from the vortex dynamics in these experiments. What is most intriguing about the results is the relatively rich structure of the η field, even though the structure of the tangential momentum field is for the most part unremarkable.

b. Development sensitivity to vertical heating distribution

Although in the middle stages of the model vortex evolution, η exhibits a relatively uniform vertical dis-

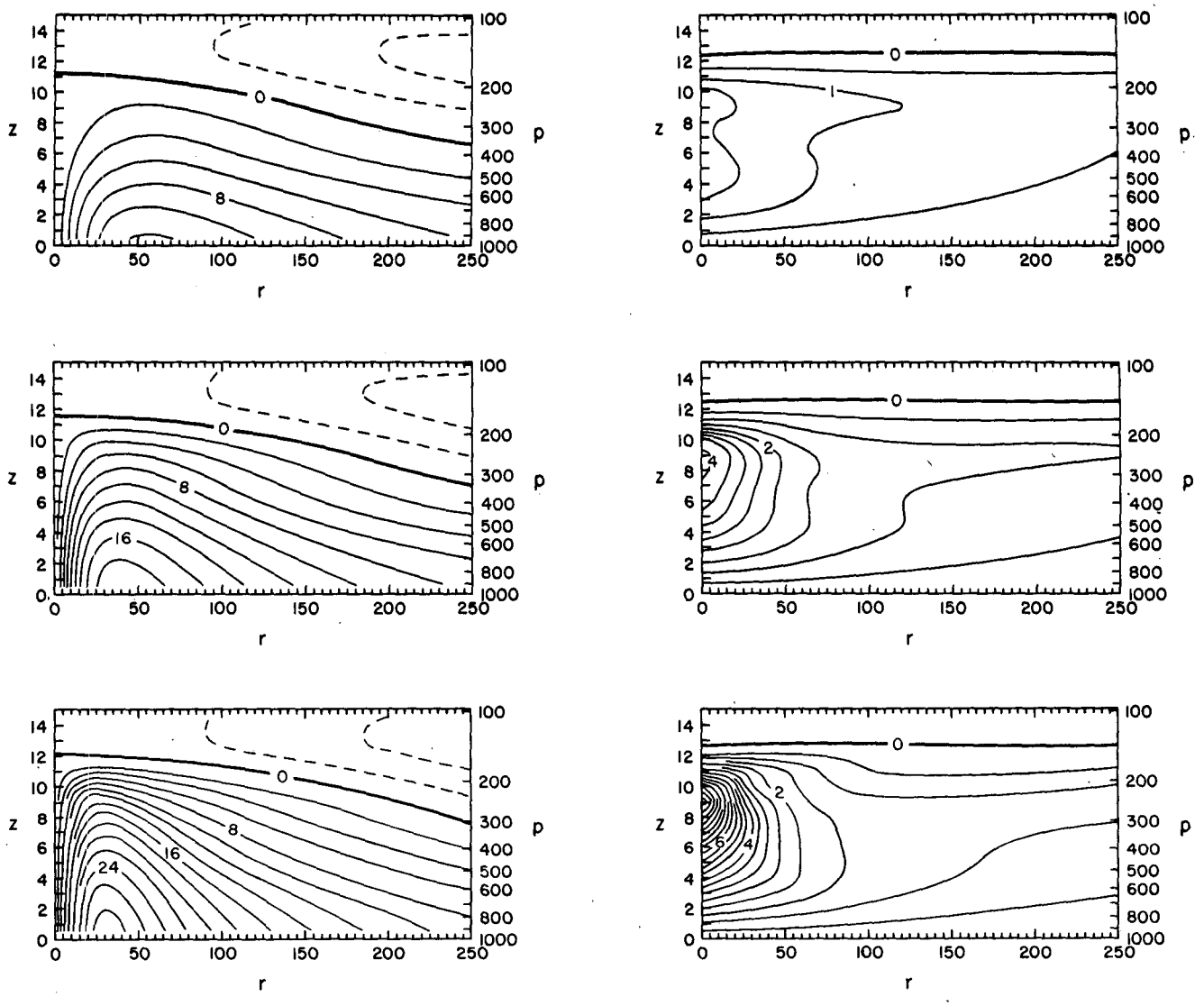

FIG. 5. Tangential momentum (left set of panels) and dynamic efficiency factor $\eta(r, z)$ in the region $r = 0$ to $r = 250$ km at 72, 96 and 120 hours for the invariantly forced balance model. The contour interval is 2 m s^{-1} for the momentum field and 0.5 percent for the dynamic efficiency factor. Negative values are denoted by dashed lines. See text for further discussion.

tribution in the interior regions, the early and late stages tend to favor a maximum η in the upper troposphere between 9 and 10 km (between 250 and 300 mb). This implies that the vortex is not necessarily as efficient as it could be at converting total potential energy to kinetic energy in these regions since the vertical distribution of the prescribed heating has its maximum amplitude some 200 mb lower in the atmosphere. This observation prompted two additional numerical experiments to assess the sensitivity of our model vortex development (and the structure of the η field) to the vertical distribution of the heating. We elected to rearrange the prescribed heating so that the vertically integrated value would remain constant. The two heating distributions we chose to examine had maximum amplitudes at 400 mb (z = 7.1 km) and 600 mb (z = 4.2 km). These profiles can be generated using values of $\hat{Q}$ = 13.8°C day^{-1}, α = 1.81 (400-mb peak) and $\hat{Q}$ = 4.52°C day^{-1}, α = −0.554, (600-mb peak) in Eq. (1.7).

The results of the two experiments were somewhat counterintuitive since the experiment with a heating maximum at 400 mb (closer to the preferred amplitude maximum for η in the previous example) develops very slowly, while the experiment with a heating maximum at 600 mb develops considerably more rapidly than the control experiment (see Fig. 3). The most astonishing aspect of these experiments, however, was that such small changes in the vertical structure of the heating could produce such large differences in the model vortex development. Other investigations have also suggested that the development of both tropical and extratropical vortices is dependent on the vertical

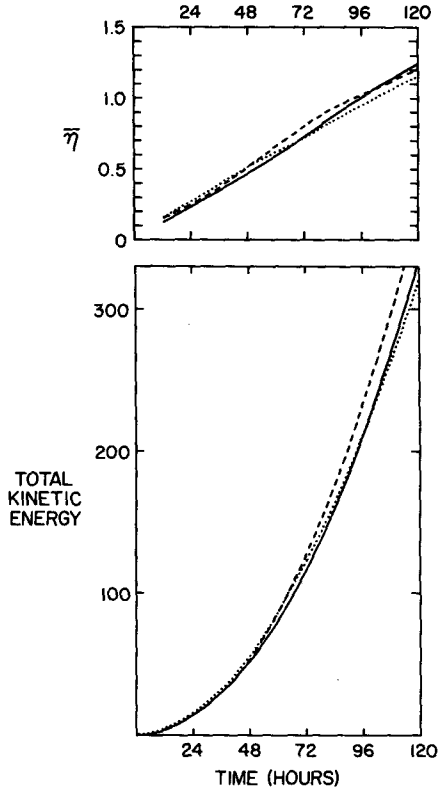

FIG. 6. Time evolution of the system efficiency parameter $\bar{\eta}$ (percent) and the total kinetic energy ($\times 10^{14}$ J) for the invariantly forced balance system. Dotted lines correspond to a maximum forcing at 400 mb, solid lines correspond to maximum forcing at 500 mb, and dashed lines correspond to maximum forcing at 600 mb.

structure of the diabatic heating, although these studies generally made use of models with very crude vertical resolution making it difficult to determine the degree of sensitivity (e.g., Yamasaki, 1968; Ooyama, 1969; Koss, 1976; Anthes, 1977; Anthes and Keyser, 1979; Anthes et al., 1983). The projection of the three heating profiles onto the vertical normal modes (see Appendix) showed only modestly different amplitude spectra, but a clear tendency for more amplitude in the higher order modes as the peak in the heating was moved lower in the troposphere. Since there is this tendency for more energy to be projected onto modes with smaller Rossby radii, as the heating maximum is moved lower into the troposphere, it could be argued (from a linear point of view) that the dynamic response to the forcing should be expected to become more radially confined as well. If such an argument were to be qualitatively correct, we might not then expect to see significant differences in the time evolution of the system efficiency $\bar{\eta}$. This is indeed the case, since the system efficiency grows in a very similar way for all three vortices, as does the kinetic energy (see Fig. 6) despite large differences in the central core development. Consequently, for this particular set of experiments, in an integrated sense the model vortices look quite similar to one another, even though their detailed structure is clearly quite different.

It is worthwhile to examine the time evolution of η in the interior for each of these experiments as shown in Fig. 7. Upper-level heating produces a vortex with a pronounced peak in the dynamic efficiency factor near $z = 10$ km that simply grows in amplitude, i.e., the vertical structure remains unchanged. In the case of lower-level heating, the vortex that is generated yields a more uniformly distributed profile of η (slightly bimodal) in the early stages of development. This profile quickly gives way to a unimodal structure for which the maximum amplitude grows rapidly with time as it moves upward through the troposphere. The middle-level (or 500 mb) heating experiment produces results somewhere between. This figure is meant to show that, although the system efficiency $\bar{\eta}$ is very similar throughout the development of all three model vortices, the distribution of $\eta(r, z)$ is considerably different. Note that, in the case of upper-level heating, η has relatively low amplitude and is confined to a fairly shallow atmospheric layer, resulting in low conversion of potential to kinetic energy (in a vertically integrated sense). The vertical distribution of the dynamic efficiency factor associated with the vortex generated by lower-level heating has much larger amplitude, much greater vertical extent, and in fact becomes phase locked with the heating profile in the middle stages of development maximizing this energy conversion. This figure suggests that for these three examples the distribution of the dynamic efficiency factor in (r, z) space is a far more useful diagnostic than our global measure of efficiency with respect to determining how rapidly a vortex might develop.

We wish to make one final observation regarding the two-dimensional structure of the efficiency factor in each of these experiments. The distribution of tangential momentum and the associated η field is shown in Fig. 8 for the point in time at which each of the model vortices achieves a maximum low-level tangential wind of approximately 15 m s^{-1}. The experiment with upper-level heating achieves this intensity at 120 hours, middle-level heating at 84 hours, and the low-level heating at 60 hours. Although parametrically equal in intensity, these vortices are quite different in their two-dimensional structure as noted earlier. The vortex generated by the upper-level heating is quite deep and relatively diffuse in the lower troposphere, while the vortex produced by the lower-level heating tends to be more shallow and tightly organized. Note that the vertical location of the maximum in η appears to be associated with the location of the greatest vertical wind shear. Since the vortex is in thermal wind balance, this region of peak shear is also associated with a maximum in the radial gradient of θ, which appears (in transformed space) on the right-hand side of the elliptic equation that determines χ^* from which the dynamic efficiency factor η is computed.

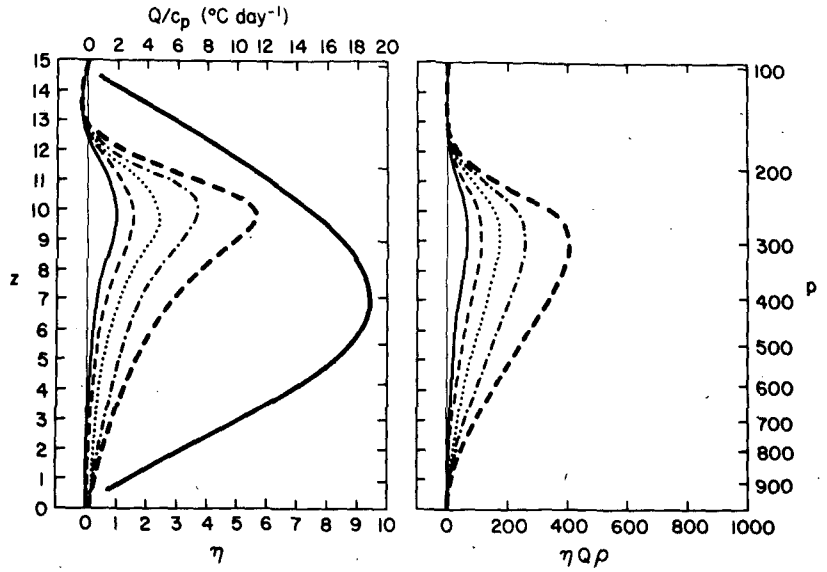
Q/cp (°C day-1)
0 2 4 6 8 10 12 14 16 18 20
z
0 1 2 3 4 5 6 7 8 9 10
η
0 200 400 600 800 1000
ηQρ
100 200 300 400 500 600 700 800 900
p

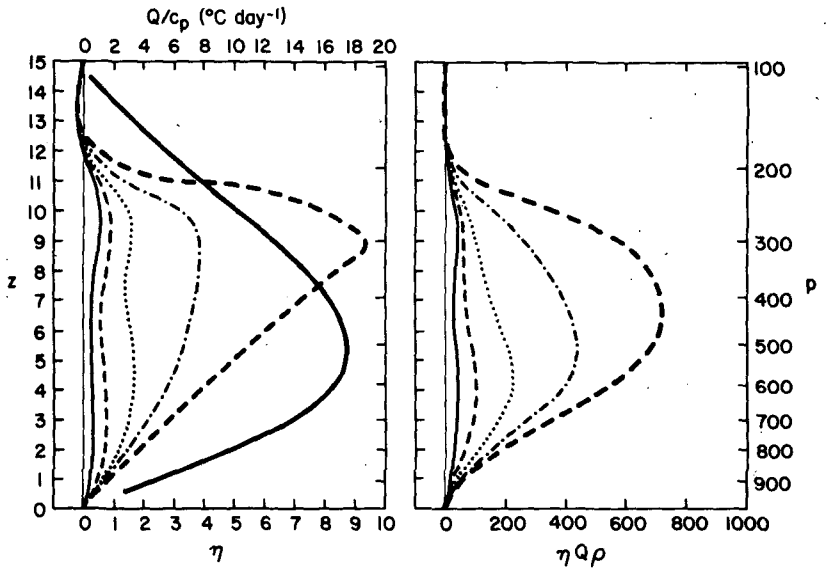
Q/cp (°C day-1)
0 2 4 6 8 10 12 14 16 18 20
z
0 1 2 3 4 5 6 7 8 9 10
η
0 200 400 600 800 1000
ηQρ
100 200 300 400 500 600 700 800 900
p

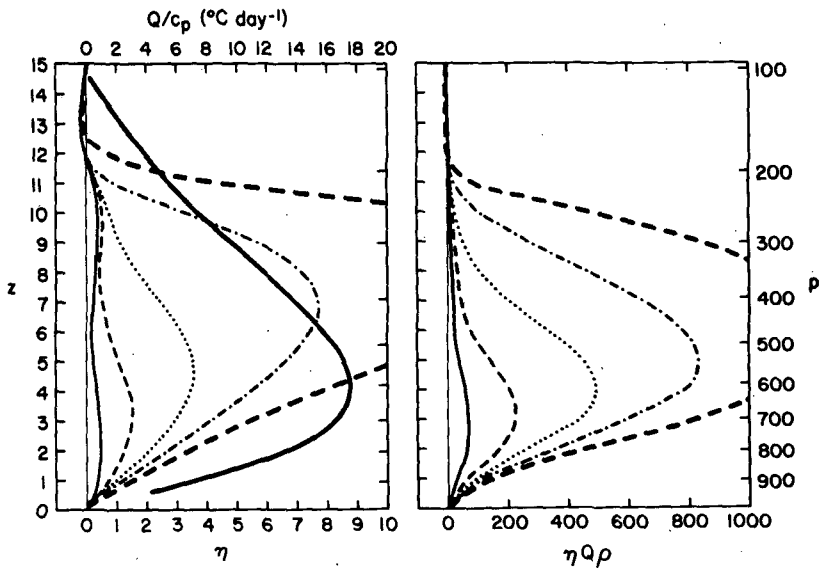
Q/cp (°C day-1)
0 2 4 6 8 10 12 14 16 18 20
z
0 1 2 3 4 5 6 7 8 9 10
η
0 200 400 600 800 1000
ηQρ
100 200 300 400 500 600 700 800 900
p

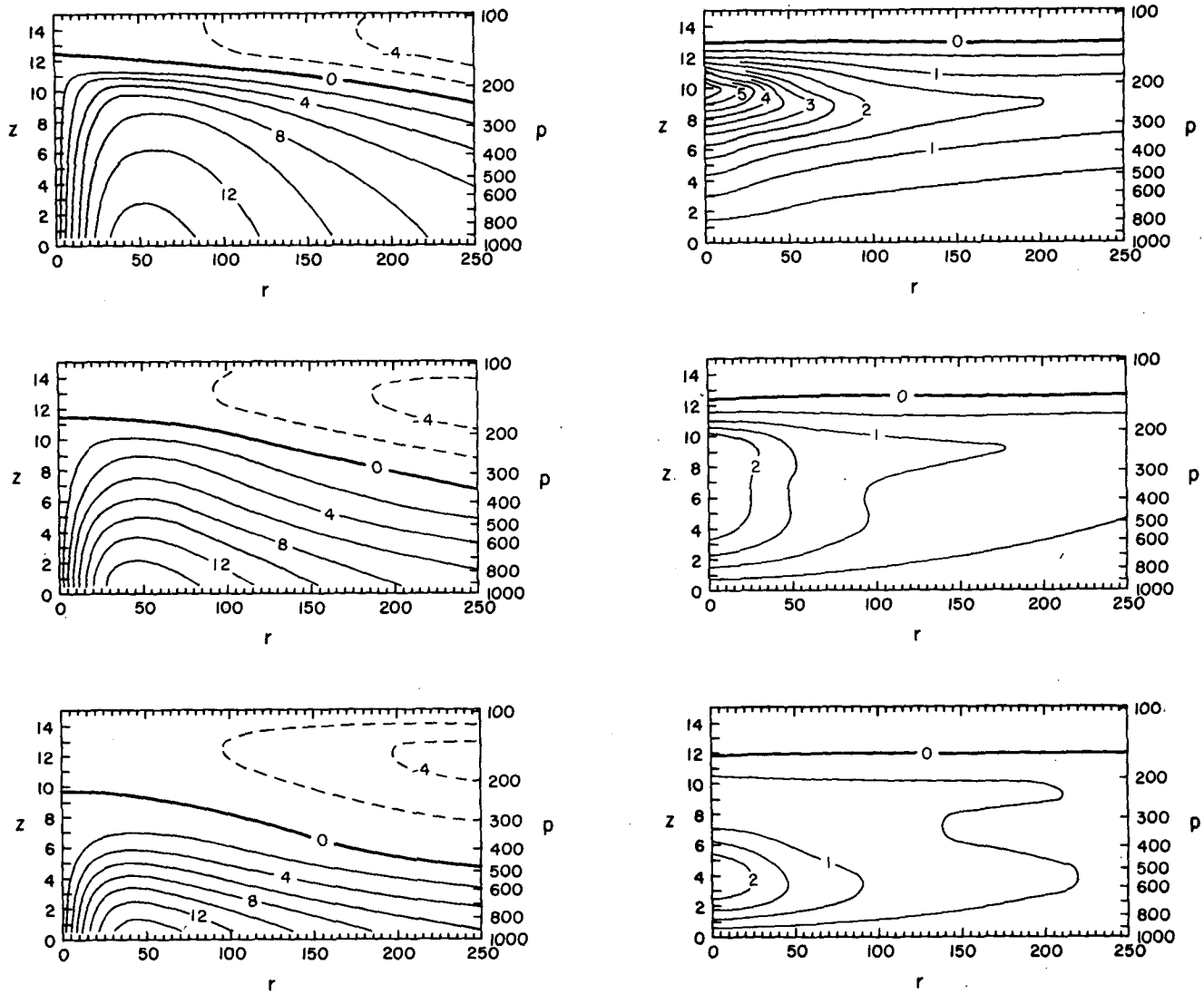

FIG. 8. Tangential wind (left panels) and dynamic efficiency factor $\eta(r, z)$ for 400 mb maximum heating at 120 hours (top row), 500 mb maximum heating at 84 hours (middle row), and 600 mb maximum heating at 60 hours (bottom row) in the region $r = 0$ to $r = 250$ km. Each vortex has a maximum low-level tangential wind of 15 m s^{-1}, where the contour interval is 2 m s^{-1} for the wind field and 0.5 percent for $\eta(r, z)$.

c. *Development sensitivity to horizontal heating distribution*

In the previous subsection, we saw a large sensitivity of the inner-core development to small changes in the vertical structure of the imposed heating, even though in an integrated sense the vortices were energetically quite similar. In this section, we examine the sensitivity of model vortex development to variations in the horizontal distribution of the heating. As we saw in the previous set of numerical experiments, each of the vortex structures has a maximum dynamic efficiency factor in the inner-core region, the same region where the diabatic heat source is a maximum. Therefore, we were motivated to conduct the following set of experiments to examine the development characteristics of a model vortex where the heating distribution has a maximum some distance from the center of the computational

FIG. 7. The left panels show the vertical distribution of the heating profile $\mathbf{Q}(0, z)/c_p$ (heavy solid lines), and the dynamic efficiency factor $\eta(0, z)$ (percent), and the panels on the right show the quantity $\eta\mathbf{Q}\rho$ (J m^{-3} s^{-1}), where the area under these curves is proportional to the vertically integrated contribution to the total energy conversion, at 24 (solid), 48 (dashed), 72 (dotted), 96 (dash-dotted) and 120 (heavy dashed) hours for the invariantly forced balance system.

domain. We elected to distribute the heating using the analytic relation

$$\frac{\mathbf{Q}}{c_p}(r, z) = aQ_1(z)\frac{r}{r_0}e^{\frac{1}{2}[1-(r/r_0)^2]}, \tag{4.1}$$

and examined heating distributions with $r_0 = 100$, 150 and 200 km. One of the problems in redistributing the forcing in the horizontal is that it becomes more difficult to maintain an integral constraint similar to our earlier experiments. Therefore, we have used a normalization so that for $r_0 = 100$ km the area-averaged heating inside 250 km is the same as the area-averaged heating inside 250 km in the previous examples. This choice leads to a slight increase of less than 5 percent in the domain-averaged heating with respect to the earlier experiments. For the remaining two experiments ($r_0 = 150$ and 200 km), the normalization coefficient a is chosen so that the domain-averaged heating is equivalent to the domain-averaged heating for the $r_0 = 100$ km case. The resulting horizontal heating distributions are contrasted with the horizontal heating distribution for the earlier set of experiments in Fig. 9. The maximum amplitude in the vertical distribution of the heating profile is at 500 mb in all cases. Note that, as r_0 is increased, more of the total heating is removed from the interior regions of the computational domain.

The three numerical experiments yield vastly different solutions in every regard. For the case $r_0 = 100$ km, the model vortex develops a peak low-level tangential wind of just over 16 m s^{-1}, as the radius of maximum wind collapses from 200 to 100 km. When $r_0 = 150$ km, the vortex attains a maximum tangential wind of almost 8 m s^{-1} while the radius of maximum wind collapses from 300 to 220 km. And for the simulation where $r_0 = 200$ km, we generate a vortex that reaches a mere 5 m s^{-1} maximum tangential wind as the radius of maximum wind collapses from 400 to 350 km. In contrast to the earlier results, we observe a distinctly dissimilar behavior in the time evolution of the system efficiency $\bar{\eta}$ for each of the experiments. These results are shown in Fig. 10 in which we have also included the result of an earlier middle-level heating experiment for purposes of comparison. Note both differences in the slope of the resulting $\bar{\eta}$ curves, as well as a clear separation at all times. Although the total diabatic heating is equivalent in each of these experiments (and nearly identical to the earlier set), the conversion of total potential energy to the kinetic energy of the balanced flow becomes much less efficient as the heating is removed from the region where the vortex develops the highest dynamic efficiency factor. In this case, the system efficiency parameter $\bar{\eta}$ becomes a much better discriminator between a rapidly developing vortex and a more slowly developing vortex.

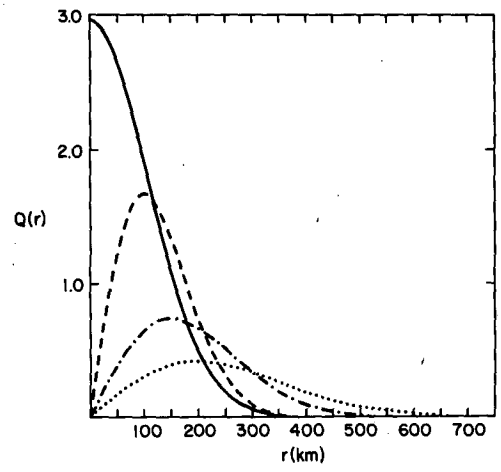

FIG. 9. Radial distribution of the diabatic heat source used in numerical results of section 4. Peaks in heating occur at $r = 0$ km (solid), $r = 100$ km (dashed), $r = 150$ km (dash-dotted), and $r = 200$ km (dotted). See text for additional discussion.

5. Concluding remarks

We have presented a mathematical argument that relates the efficiency of a large-scale atmospheric vortex to the instantaneous global structure of the tangential momentum field for balanced, inviscid, axisymmetric flow. By integrating the transformed balanced system of equations forced with an invariant diabatic heat source, we have demonstrated that a vortex becomes more efficient at converting total potential energy to balanced rotational motion as it increases in intensity. This increase in efficiency, a consequence of the increasing potential vorticity, inertial stability, and radial temperature gradient of the intensifying vortex circulation, results in a nonlinear instability of the vortex for a specified diabatic forcing. That is, the dynamic efficiency factor depends totally upon the immediate state of the large-scale circulation, which in turn evolves in response to the relative positions of this efficiency field and the specified diabatic forcing.

Two useful diagnostic parameters, the dynamic efficiency factor $\eta(r, z, t)$ and the system efficiency $\bar{\eta}(t)$, were introduced in section 3, and were utilized in the analysis of the numerical experiments conducted in section 4. The global parameter $\bar{\eta}(t)$ is apparently most suitable for interpreting whether an optimal orientation of the diabatic heating field and dynamic efficiency factor exists. The distribution of the dynamic efficiency factor appears to be most valuable in determining the detailed structure of the dynamic response, given knowledge of the diabatic heating distribution. An interesting application of these concepts would be to compute values of $\eta(r, z, t)$ and $\bar{\eta}(t)$ from actual observations, especially during a concentric eyewall cycle as described by Willoughby et al. (1982).

In addition to providing insight into the time evolution of the dynamic efficiency factor and system efficiency, the numerical experiments conducted in section 4 yielded additional evidence that the dynamic

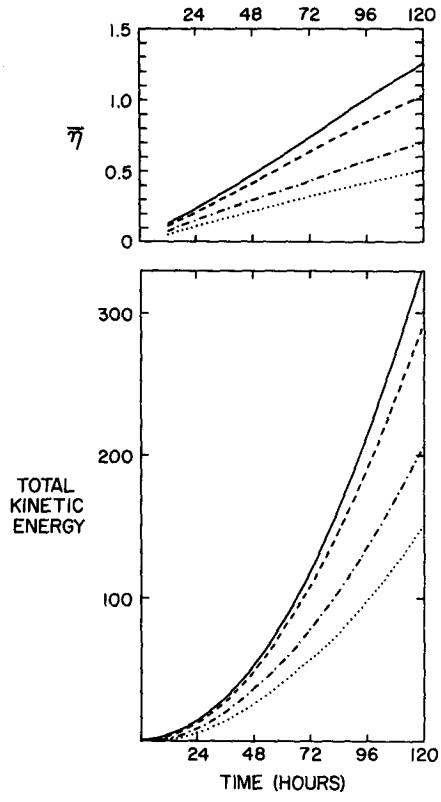

FIG. 10. Time evolution of the system efficiency parameter $\bar{\eta}$ (percent) and the total kinetic energy ($\times 10^{14}$ J) for the invariantly forced balance system. Dotted lines correspond to a maximum forcing at 200 km, dash-dotted lines correspond to maximum forcing at 150 km, dashed lines correspond to maximum forcing at 100 km, and the solid lines correspond to a maximum forcing at the origin and are included for comparison with Fig. 6.

response to a diabatic heat source is strongly dependent on the vertical distribution of the heat source. Interestingly, the total conversion of potential to kinetic energy appears to be independent of the vertical structure of the heating, as seen in the time evolution of the system efficiency parameter. The horizontal scale of the dynamic response, however, is extremely sensitive to the vertical distribution of the heat source where the response becomes more localized when the heating has a larger projection onto higher order vertical normal modes.

It is a bit discouraging that small changes in the diabatic heating profile can have such a profound impact on the evolution of the large-scale flow when one considers the current state of cumulus parameterization theory. Our results certainly underscore the need to develop a deeper understanding of the physical processes that determine the convective-scale response to large-scale forcing so that they may be incorporated in cumulus parameterization schemes. This response takes the form of a direct feedback to the large-scale flow through cumulus-scale flux divergence and source/sink terms. In addition to the direct action of the clouds, it is also essential to describe accurately their impact on the large-scale radiation fields since their radiative properties could certainly prove to have an important modulating effect on the vertical distribution of the diabatic heating (e.g., Albrecht and Cox, 1975).

It is evident that the development of tropical vortices is considerably more complex than can be explained by linear theory. Although many of the conceptual elements of early linear attempts to understand tropical cyclone formation are surely qualitatively valid, nonlinear processes clearly begin to dominate the characteristics of tropical cyclone development at a very early stage. We would hope that, by generalizing these results to accommodate three-dimensional curved flow, it might be possible to understand better many of the yet unresolved mysteries of hurricane structure and formation.

Acknowledgments. We wish to thank Paul Ciesielski, Scott Fulton, Mark DeMaria and Richard Anthes for their helpful comments throughout the course of this work, and Ann Modahl, Stephanie Honaski and Melanie Pappas for their assistance in the preparation of this manuscript. This work was supported in part by the National Science Foundation under Grant ATM-8207563.

APPENDIX

Numerical Methods

The numerical integration of the transformed balance system is accomplished using a finite-difference method. The radial domain is divided into I equal intervals separated by the $I + 1$ points $R_i = i\Delta R$ ($i = 0, 1, 2, \cdots I$), while the vertical domain is divided into J equal intervals separated by the $J + 1$ points $Z_j = j\Delta Z$ ($j = 0, 1, 2, \cdots J$). Staggered with respect to the i, j points are the points $R_{i+1/2} = (i + 1/2)\Delta R$ and $Z_{j+1/2} = (j + 1/2)\Delta Z$. The distribution of the variables over these points is shown in Fig. 11. The inner ($i = 0$) and outer ($i = I$) boundaries are columns along

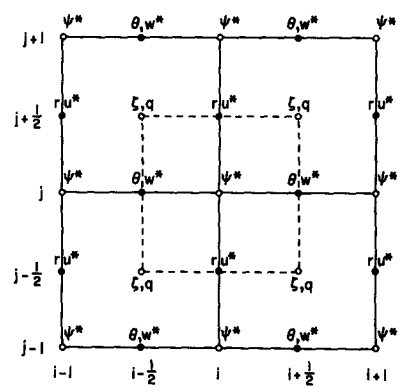

FIG. 11. Finite-difference grid for solution of the transformed balance system of equations.

which r, u^* and ψ^* are defined, while the lower ($j = 0$) and upper ($j = J$) boundaries are levels where θ, w^* and ψ^* are defined. In all the integrations presented here, we have chosen $I = 50$, $J = 15$, $\Delta R = 20$ km, and $\Delta Z = 1$ km.

The solution procedure is to evaluate the θ and ζ fields from the time-dependent variable r using the thermal wind relation,

$$-f^2 \frac{R^3}{r^3}\frac{\partial r}{\partial Z} = \frac{g}{\theta_0}\frac{\partial \theta}{\partial R},$$

and (2.12), diagnose potential vorticity q, and inertial stability s using (2.24), solve for the transverse circulation ψ^* using (2.26), diagnose the transverse circulation components using (2.25), and finally predict new values of r using (2.7). In finite-difference form, these equations can be written

$$\theta_{i-1/2,j} = \theta_{i+1/2,j} - \frac{f^2\theta_0\Delta R}{2g\Delta Z} R_i^3(r_{i,j+1/2}^{-2} - r_{i,j-1/2}^{-2}), \quad \text{(A1)}$$

$$\zeta_{i+1/2,j+1/2} = f\frac{(R_{i+1}^2 - R_i^2)}{(r_{i+1,j+1/2}^2 - r_{i,j+1/2}^2)}, \quad \text{(A2)}$$

$$(\rho q)_{i+1/2,j+1/2} = \zeta_{i+1/2,j+1/2}\left(\frac{g}{f\theta_0\Delta Z}\right)(\theta_{i+1/2,j+1} - \theta_{i+1/2,j}), \quad \text{(A3)}$$

$$(\rho s)_{i,j+1/2} = f^2\left(\frac{R_i^4}{r_{i,j+1/2}^4}\right), \quad \text{(A4)}$$

$$\begin{aligned} &a_{i-1/2,j}\psi^*_{i-1,j} + a_{i+1/2,j}\psi^*_{i+1,j} + b_{i,j-1/2}\psi^*_{i,j-1} \\ &\quad + b_{i,j+1/2}\psi^*_{i,j+1} - [R_i^{1/2}(R_{i-1}^{-1/2}a_{i-1/2,j} + R_{i+1}^{-1/2}a_{i+1/2,j}) \\ &\quad + \rho_j^{1/2}(\rho_{j-1}^{-1/2}b_{i,j-1/2} + \rho_{j+1}^{-1/2}b_{i,j+1/2})]\psi^*_{i,j} \\ &\qquad = \frac{g}{\theta_0}\left(\rho^{1/2}R^{1/2}\frac{\partial Q}{\partial R}\right)_{i,j}\Delta R\Delta Z \end{aligned}$$

where

$$a_{i-1/2,j} = \frac{\Delta Z}{\Delta R}\frac{R_{i-1}^{1/2}R_i^{1/2}}{R_{i-1/2}} \times \frac{1}{2}[(\rho q)_{i-1/2,j-1/2} + (\rho q)_{i-1/2,j+1/2}],$$

$$b_{i,j-1/2} = \frac{\Delta R}{\Delta Z}\frac{\rho_{j-1}^{1/2}\rho_j^{1/2}}{\rho_{j-1/2}}(\rho s)_{i,j-1/2}, \quad \text{(A5)}$$

and

$$\frac{\partial r_{i,j+1/2}}{\partial T} = \frac{2R_i}{\rho_{j+1/2}\Delta Z}(\psi^*_{i,j} - \psi^*_{i,j+1}). \quad \text{(A6)}$$

The elliptic equation for the transverse circulation ψ^* (A5) is solved using a red–black successive overrelaxation procedure. A multigrid approach to the solution of this equation has also been implemented and is discussed in some detail in Ciesielski et al. (1986).

Our lateral boundary condition is based on the far-field solution of the transverse circulation equation and is derived as follows. At large R, we assume that $Q \approx 0$, $\zeta \approx f$, $\rho q \approx (g/\theta_0)(\partial\theta/\partial Z) = N^2(Z)$, and $\rho s \approx f^2$. For such a situation, the transverse circulation equation becomes

$$\frac{N^2}{\rho f^2}\frac{\partial}{\partial R}\left(\frac{\partial R\psi^*}{R\partial R}\right) + \frac{\partial}{\partial Z}\left(\frac{\partial\psi^*}{\rho\partial Z}\right) = 0. \quad \text{(A7)}$$

If we discretize in Z but remain continuous in R, we obtain

$$\frac{\rho_0}{\rho_j}\frac{(N_j\Delta Z)^2}{f^2}\frac{\partial}{\partial R}\left(\frac{\partial R\psi_j^*}{R\partial R}\right) - \left\{-\left(\frac{\rho_0}{\rho_{j-1/2}}\right)\psi^*_{j-1} + \left(\frac{\rho_0}{\rho_{j-1/2}} + \frac{\rho_0}{\rho_{j+1/2}}\right)\psi_j^* - \left(\frac{\rho_0}{\rho_{j+1/2}}\right)\psi^*_{j+1}\right\} = 0, \quad \text{(A8)}$$

for $j = 1, 2, \cdots J$ with boundary conditions $\psi_0^* = \psi_{J+1}^* = 0$. In order to express (A8) in vector form, let us define $\underset{\sim}{\psi}^* = [\psi_1^*, \psi_2^*, \cdots \psi_J^*]^T$, the diagonal static stability matrix by $\mathbf{S} = \rho_0(\Delta Z)^2 \operatorname{diag}[N_1^2/\rho_1, N_2^2/\rho_2, \cdots N_J^2/\rho_J]$ and the symmetric tridiagonal "density" matrix by $\mathbf{D}$. Then (A8) can be written

$$\frac{1}{f^2}\frac{\partial}{\partial R}\left(\frac{\partial R\mathbf{S}\underset{\sim}{\psi}^*}{R\partial R}\right) - \mathbf{D}\underset{\sim}{\psi}^* = 0. \quad \text{(A9)}$$

Now consider the generalized eigenvalue problem

$$\mathbf{SZ} = c^2\mathbf{DZ}. \quad \text{(A10)}$$

Since $\mathbf{S}$ and $\mathbf{D}$ are real, symmetric, and positive definite, the eigenvalues $c_1^2, c_2^2, \ldots, c_J^2$ are real and positive, and the eigenvectors are orthonormal in the sense that

$$\mathbf{Z}_m^T\mathbf{D}\mathbf{Z}_n = \begin{cases} 1, & m = n \\ 0, & m \neq n. \end{cases} \quad \text{(A11)}$$

Thus, we can write the vertical transform pair as

$$\underset{\sim}{\psi}^* = \sum_{m=1}^{J}\hat{\psi}_m^*\mathbf{Z}_m, \quad \text{(A12)}$$

$$\hat{\psi}_m^* = \mathbf{Z}_m^T\mathbf{D}\underset{\sim}{\psi}^*. \quad \text{(A13)}$$

Equation (A13) is the transformation from vertical level space to vertical normal mode space and (A12) is the transformation back. We now vertically transform (A9) by multiplying by $\mathbf{Z}_m^T$ and using (A10)–(A13) to obtain

$$R^2\frac{d^2\hat{\psi}_m^*}{dR^2} + R\frac{d\hat{\psi}_m^*}{dR} - (\mu_m^2R^2 + 1)\hat{\psi}_m^* = 0, \quad \text{(A14)}$$

where $\mu_m = f/c_m$. The solution of (A14) is a linear combination of the decaying function $K_1(\mu_m R)$, and the growing function $I_1(\mu_m R)$. We can simulate an infinite domain by enforcing a condition which eliminates the $I_1(\mu_m R)$ solution. As discussed in Schubert and Hack (1983), such a condition is

$$\frac{dR\hat{\psi}_m^*}{RdR} + \lambda_m\hat{\psi}_m^* = 0 \quad \text{at} \quad R = \hat{R}, \quad \text{(A15)}$$

where

$$\lambda_m = \frac{\mu_m K_0(\mu_m\hat{R})}{K_1(\mu_m\hat{R})}.$$

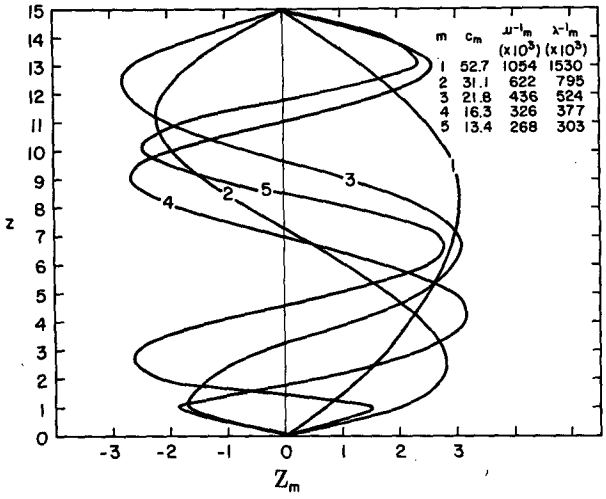

FIG. 12. Vertical structure functions $\mathbf{Z}_m$ and associated phase speeds c_m, Rossby radii μ_m^{-1}, and boundary scales λ_m^{-1}, calculated using the mean Marshall Islands thermodynamic profile obtained by Yanai et al. (1973).

We now wish to transform (A15) back into physical space and then discretize it in R. Multiplying (A15) by $\mathbf{Z}_m$, summing over m, using (A12)–(A13), and taking a one-sided difference in R, we obtain

$$\underset{\sim}{\psi}^*_{I+1} = \frac{R_I}{R_{I+1}} \{\underset{\sim}{\psi}^*_I + \Delta R \sum_{m=1}^{J} \lambda_m \mathbf{Z}_m^T \mathbf{D} \underset{\sim}{\psi}^*_I \mathbf{Z}_m\}, \quad \text{(A16)}$$

which links every point in the boundary column $i = I + 1$ to every point in the neighboring column $i = I$. The basis vectors $\mathbf{Z}_m$ are easily determined from the numerical solution of the generalized eigenvalue problem (A10). The first few basis vectors, along with their associated phase speeds c_m, Rossby radii μ_m^{-1}, and boundary scales λ_m^{-1} are shown in Fig. 12. These solutions were computed using a mean tropical sounding for $N^2(Z)$, $\Delta Z = 1$ km, $f = 5 \times 10^{-5}$ s^{-1}, and $\hat{R} = 1000$ km.

REFERENCES

Albrecht, B. A., and S. K. Cox, 1975: The large-scale response of the tropical atmosphere to cloud-modulated infrared heating. *J. Atmos. Sci.*, **32**, 16–24.

Anthes, R. A., 1977: Hurricane model experiments with a new cumulus parameterization scheme. *Mon. Wea. Rev.*, **107**, 287–300.

——, and D. Keyser, 1979: Tests of a fine-mesh model over Europe and the United States. *Mon. Wea. Rev.*, **107**, 963–984.

——, Y.-H. Kuo and J. R. Gyakum, 1983: Numerical simulations of a case of explosive marine cyclogenesis. *Mon. Wea. Rev.*, **111**, 1174–1188.

Ciesielski, P. E., S. R. Fulton and W. H. Schubert, 1986: Multigrid solution of an elliptic boundary value problem from tropical cyclone theory. *Mon. Wea. Rev.*, **114**, 797–807.

Charney, J. G., and A. Eliassen, 1964: On the growth of the hurricane depression. *J. Atmos. Sci.*, **21**, 68–75.

Eliassen, A., 1952: Slow thermally or frictionally controlled meridional circulation in a circular vortex. *Astrophys. Norv.*, **5**, 60 pp.

Gill, A. E., 1981: Homogeneous intrusions in a rotating stratified fluid. *J. Fluid Mech.*, **103**, 275–295.

Gray, W. M., 1981: *Recent Advances in Tropical Cyclone Research from Rawinsonde Composite Analysis.* WMO, 407 pp.

Hack, J. J., 1980: The role of convective-scale processes in tropical cyclone development. Ph.D. dissertation, Colorado State University, 206 pp. [University Microfilms Order No. 8110808.]

——, and W. H. Schubert, 1981: Lateral boundary conditions for tropical cyclone models. *Mon. Wea. Rev.*, **109**, 1404–1420.

Holliday, C. R., and A. H. Thompson, 1979: Climatological characteristics of rapidly intensifying typhoons. *Mon. Wea. Rev.*, **107**, 1022–1034.

Hoskins, B. J., and F. P. Bretherton, 1972: Atmospheric frontogenesis models: Mathematical formulation and solution. *J. Atmos. Sci.*, **29**, 11–37.

——, and I. Draghici, 1977: The forcing of ageostrophic motion according to the semigeostrophic equations and in an isentropic coordinate model. *J. Atmos. Sci.*, **34**, 1859–1867.

Johnson, D. R., 1970: The available potential energy of storms. *J. Atmos. Sci.*, **27**, 727–741.

Koss, W. J., 1976: Linear stability of CISK-induced disturbances: Fourier component eigenvalue analysis. *J. Atmos. Sci.*, **33**, 1195–1222.

Kurihara, Y., and R. E. Tuleya, 1974: Structure of a tropical cyclone developed in a three-dimensional numerical simulation model. *J. Atmos. Sci.*, **31**, 893–919.

Lorenz, E. N., 1967: The nature and theory of the general circulation of the atmosphere. WMO No. 218, TP. 115, 161 pp.

Ooyama, K., 1964: A dynamical model for the study of tropical cyclone development. *Geofis. Int.*, **4**, 187–198.

——, 1969a: Numerical simulation of the life cycle of tropical cyclones. *J. Atmos. Sci.*, **26**, 3–40.

——, 1969b: Numerical simulation of tropical cyclones with an axisymmetric model. *Proc. WMO/IUGG Symp. on Numerical Weather Prediction*, Tokyo, 1968, III: 81–88.

——, 1982: Conceptual evolution of the theory and modeling of the tropical cyclone. *J. Meteor. Soc. Japan*, **60**, 369–379.

Schubert, W. H., and J. J. Hack, 1982: Inertial stability and tropical cyclone development. *J. Atmos. Sci.*, **39**, 1687–1697.

——, and ——, 1983: Transformed Eliassen balanced vortex model. *J. Atmos. Sci.*, **40**, 1571–1583.

——, J. J. Hack, P. L. Silva Dias and S. R. Fulton, 1980: Geostrophic adjustment in an axisymmetric vortex. *J. Atmos. Sci.*, **37**, 1464–1484.

——, P. Ciesielski and J. J. Hack, 1984: Response of the tropical atmosphere to convective cloud clusters. *Proc. ECMWF Workshop on Convection in Large-Scale Models*, ECMWF, Reading, 377–390.

Shapiro, L. J., and H. E. Willoughby, 1982: The response of balanced hurricanes to local sources of heat and momentum. *J. Atmos. Sci.*, **39**, 378–394.

Shutts, G. J., 1980: Angular momentum coordinates and their use in zonal, geostrophic motion in a hemisphere. *J. Atmos. Sci.*, **37**, 1126–1132.

——, and A. J. Thorpe, 1978: Some aspects of vortices in rotating, stratified fluids. *Pure Appl. Geophys.*, **116**, 993–1006.

Silva Dias, P. L., W. H. Schubert and M. DeMaria, 1983: Large-scale response of the tropical atmosphere to transient convection. *J. Atmos. Sci.*, **40**, 2689–2707.

Sundqvist, H., 1970: Numerical simulation of the development of tropical cyclones with a ten-level model, I. *Tellus*, **22**, 359–390.

Thorpe, A. J., 1985: Diagnosis of balanced vortex structure using potential vorticity. *J. Atmos. Sci.*, **42**, 397–406.

Willoughby, H. E., J. A. Clos and M. G. Shoreibah, 1982: Concentric eye walls, secondary wind maxima, and the evolution of the hurricane vortex. *J. Atmos. Sci.*, **39**, 395–411.

Yamasaki, M., 1968: Numerical simulation of tropical cyclone development with use of the primitive equations. *J. Meteor. Soc. Japan*, **46**, 178–201.

Yanai, M., S. Esbensen and J.-H. Chu, 1973: Determination of bulk properties of tropical cloud clusters from large-scale heat and moisture budgets. *J. Atmos. Sci.*, **30**, 611–627.